Downloaded from ascelibrary.org by Hong Kong University of Science and Technology (Guangzhou) on 08/02/24. Copyright ASCE. For personal use only; all rights reserved.

General Framework for Modeling Multifunctional Metamaterial Beam Based on a Derived One-Dimensional Piezoelectric Composite Finite Element

Guobiao Hu[1]; Lihua Tang[2]; and Raj Das[3]

Abstract: Phononic crystals and metamaterials have been widely investigated over the last decade. In recent years, by integration with piezoelectric transducers, phononic/metamaterial-based piezoelectric energy harvesters (PEHs) have gained increasing research interest for achieving multifunctionalities. This paper proposes a general framework for modelling phononic/metamaterial beams bonded with piezoelectric transducers based on a one-dimensional piezoelectric composite finite element derived using the generalized Hamilton's principle. A method for calculating band structures of infinitely long models of phononic/metamaterial beams that can carry piezoelectric transducers is then developed. This method is demonstrated via two case studies. The first case study investigates a metamaterial beam without piezoelectric coverage, and the proposed method is verified by the transfer matrix method (TMM). Compared with the TMM, the proposed method provides a dispersion relationship in a simpler form and thus demonstrates higher computational efficiency. The second case study investigates a metamaterial beam with periodic piezoelectric coverage. The proposed method takes into consideration the piezoelectric effect. Band structures of such a piezoelectric metamaterial beam under short-circuit and open-circuit conditions are evaluated. Subsequently, corresponding finitely long models of the two case studies are analyzed. The transmittances and open-circuit voltage responses of the piezoelectric transducers are then calculated. The predicted band gaps from transmittances match well with those from band structures. In addition, the transmittances and open-circuit voltage responses of piezoelectric transducers predicted based on the proposed model are verified against the finite-element solution produced by the ANSYS FE program. **DOI: 10.1061/(ASCE)AS.1943-5525.0000920.** © *2018 American Society of Civil Engineers.*

Introduction

In recent decades, the propagation of elastic or acoustic waves in materials with periodic structures, called phononic crystals (PCs), has been extensively studied (Chen et al. 2011; Lu et al. 2009; Page et al. 2004). One important characteristic of phononic crystals is the band gap generated by the mechanism of Bragg scattering due to the periodic impedance mismatch. A band gap is a frequency range within which the propagation of elastic or acoustic wave is completely obstructed. Hence, phononic crystals have been widely investigated for vibration suppression applications. However, band gaps generated by Bragg scattering are the result of the interaction among incident, reflected, and transmitted waves when the wavelength is comparable with the lattice constant. Therefore the dependence on the size of the lattice constant limits their practical applications in the low-frequency domain. In the last decade, elastic metamaterials (EMMs) with unique effective dynamic properties that cannot be realized in natural materials have received great interest (Banerjee et al. 2017; Huang et al. 2009; Yao et al. 2008). These materials can also generate band gaps, but based on local resonance mechanisms. For this reason, elastic metamaterials are also termed local resonant (LR) metamaterials. With periodically embedded local resonators in metamaterials, the band gap occurs when the external excitation frequency is near the local resonant frequency and the local resonators undergo out-of-phase motions. The dominant phenomenon in the formation of band gaps is local resonance, and thus it is irrelevant to the lattice constant. Therefore, elastic metamaterials seem more suited to be designed for low-frequency vibration suppression. To distinguish between the band gaps generated by Bragg scattering mechanism and the local resonance mechanism, this paper uses the terms Bragg gap and local resonant gap.

Beams are widely used structures in engineering designs. By integration with phononic crystals or local resonant metamaterials, the concepts of phononic beams and metamaterial beams have been proposed and studied. Based on the Euler–Bernoulli beam theory in conjunction with the transfer matrix method (TMM), Liu et al. (2007) proposed a method for calculating band structures of metamaterial beams. By replacing the Euler–Bernoulli beam theory with the Timoshenko beam theory and following the same procedure, Yu et al. (2006) proposed a similar method for calculating band structures of metamaterial beams. Pai (2010) derived the dispersion relation of a metamaterial beam by adopting another method based on the combination of the beam theory and Bloch's theorem. Under the assumption of an infinite number of resonators, Sugino et al. (2017c) proposed a novel method for estimating bands gaps of metamaterial beams based on modal analysis. In addition to methodology studies for band structure calculation, Zhu et al. (2014) developed an elastic metamaterial beam with multiple embedded local resonators for broadband vibration suppression. Multiple

---

[1] Ph.D. Student, Dept. of Mechanical Engineering, Univ. of Auckland, 20 Symonds St., Auckland 1010, New Zealand. Email: ghu211@aucklanduni.ac.nz

[2] Senior Lecturer, Dept. of Mechanical Engineering, Univ. of Auckland, 20 Symonds St., Auckland 1010, New Zealand (corresponding author). ORCID: https://orcid.org/0000-0001-9031-4190. Email: l.tang@auckland.ac.nz

[3] Associate Professor, School of Engineering, RMIT Univ., GPO Box 2476, Melbourne, VIC 3001, Australia. Email: raj.das@rmit.edu.au

Note. This manuscript was submitted on February 1, 2018; approved on April 23, 2018; published online on July 17, 2018. Discussion period open until December 17, 2018; separate discussions must be submitted for individual papers. This paper is part of the ***Journal of Aerospace Engineering***, © ASCE, ISSN 0893-1321.

J. Aerosp. Eng., 2018, 31(6): 04018088

Downloaded from ascelibrary.org by Hong Kong University of Science and Technology (Guangzhou) on 08/02/24. Copyright ASCE. For personal use only; all rights reserved.

local resonant gaps existed in their proposed metamaterial beam, as demonstrated via experimental validation. Zhang et al. (2013) designed a metamaterial beam attached with spiral resonators. They performed both numerical and experimental investigations. Chen et al. (2011) presented a piezoelectric phononic beam with active band-gap controllability. The host beam was periodically covered by piezoelectric patches that were shunted with negative capacitances. Through tuning the value of the negative capacitance, the effective Young's modulus of the piezoelectric-covered sections was varied, thus resulting in periodic impedance mismatch, whereby the band gap was controlled. All the preceding studies of band gaps of phononic or metamaterial beams were based on calculating the band structures of infinitely long models by using the transfer matrix method or the finite-element method (e.g., commercial finite-element software COMSOL). Recently, based on the finitely long model, Hu et al. (2017b) analytically studied a piezoelectric embedded metamaterial beam for simultaneous vibration suppression and energy harvesting. They provided finite-element results from ANSYS to validate their method. Similarly, based on the finitely long model, Sugino et al. (2017b) investigated a hybrid metamaterial beam with both Bragg and LR gaps. Their model was similar to that presented by Chen et al. (2011). On that basis, periodic resonators were added onto the phononic beam to create an additional LR gap. They verified their method by comparing the results with those from the plane wave expansion method.

In recent years, researchers have explored the potential of metamaterials for energy harvesting (Carrara et al. 2013; Chen et al. 2014; Hu et al. 2017a; Mikoshiba et al. 2013). For conventional piezoelectric energy harvesters (PEHs), various modeling methods have been proposed. Erturk and Inman (2008) developed an analytical distributed parameter model for unimorph/bimorph piezoelectric energy harvesters. Junior et al. (2009) derived a finite-element formulation for modeling two-dimensional plate-type piezoelectric energy harvesters. Yang and Tang (2009) proposed an equivalent circuit method for modeling piezoelectric energy harvesters. Because most effective piezoelectric energy harvesters are designed as the beam type (Erturk and Inman 2008; Shu and Lien 2006; Tang and Yang 2012; Xu and Tang 2017), the combination of metamaterials and energy harvesters also often yields beam structural designs. Shen et al. (2015) used a metamaterial beam model similar to that proposed by Zhang et al. (2013) for energy harvesting. They reported that the energy transformation could be achieved at a dozen resonant frequencies within a low frequency range. Chen et al. (2013) studied a piezoelectric phononic beam with periodically placed lumped masses. Their study focused on using this structure for vibration energy harvesting. The piezoelectric metamaterial beam proposed by Hu et al. (2017b) possessed not only vibration suppression ability but also energy harvesting functionality. They evaluated the energy harvesting performance by using an analytical method and verified it by using finite-element analysis with ANSYS. Based on a similar idea, Sugino et al. (2017a) also investigated a multifunctional metamaterial beam with piezoelectric elements. They found that the introduction of the piezoelectric elements could convert vibration-induced energy into electrical energy but it did not significantly affect the vibration suppression performance within the band gap. Research in this area is still in an emerging stage.

This paper develops a framework for modeling piezoelectric metamaterial beams for the purpose of providing a powerful analysis method for estimating their energy harvesting and vibration suppression performance. Existing methods for band structure calculation in the literature cannot consider the piezoelectric effect. Within the proposed framework, band structure studies of infinitely long phononic/metamaterial beams with piezoelectric transducers under short-circuit and open-circuit conditions can be conducted, as well as transmittance and energy harvesting performance studies of finitely long phononic/metamaterial beams. The rest of this paper is organized as follows. First, a one-dimensional (1D) two-node piezoelectric composite finite element is introduced and formulated by the generalized Hamilton's principle. Subsequently, based on the developed piezoelectric composite finite-element model, a method for modeling and analyzing infinitely long metamaterial beams with piezoelectric coverage is proposed. Two case studies are presented. The first case study investigates a pure metamaterial beam and evaluates and verifies the band structure using the proposed method by the TMM method. The second case study periodically bonds the metamaterial beam with piezoelectric transducers. Because of the impedance mismatch between the subsections with and without piezoelectric coverage, a Bragg gap forms in the beam, in addition to the LR gap. Hereinafter, this is referred to as the phononic metamaterial beam. The band structures of the phononic metamaterial beam bonded with periodic piezoelectric transducers under short-circuit and open-circuit conditions are respectively calculated. Finally, based on the derived piezoelectric composite finite element, corresponding finitely long models of the aforementioned two cases are established. Regarding the prediction of band gaps, the obtained transmittances show good agreement with the predictions from band structures. In addition, the obtained transmittances and the open-circuit voltage responses of the bonded piezoelectric transducers are also verified against the finite-element solutions by ANSYS.

Formulation of Piezoelectric Composite Finite Element

This section formulates a one-dimensional two-node piezoelectric composite finite element for beam-type PEHs (Fig. 1). This element formulation has two degrees of freedom (DOFs) at each node, namely, translation (u_1 and u_3) and rotation (u_2 and u_4). An additional degree of freedom is the voltage (v). Fig. 1 details the geometry of the composite finite element, wherein h_a and h_b are the positions of the bottom and top of the substrate layer from the neutral axis, respectively, h_c is the position of the top of the piezoelectric layer from the neutral axis, h_s is the thickness of the

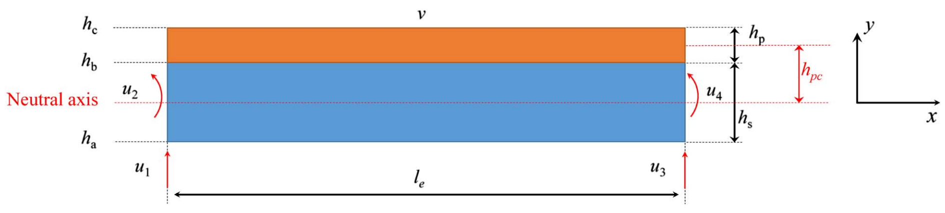

Fig. 1. 1D two-node piezoelectric composite finite element with four mechanical DOFs and one electric DOF.

substrate layer, h_p is the thickness of the piezoelectric layer, and l_e is the length of the composite element.

The nodal displacement vector of the element consists of four components $\mathbf{u}_e = [\,u_1(t) \quad u_2(t) \quad u_3(t) \quad u_4(t)\,]^T$, and thus cubic interpolation functions are used to represent the vertical displacement in the element. The vertical displacement in the element can be interpolated by four nodal displacements

$$u(\xi,t) = \mathbf{\Phi}^T\mathbf{u}_e = [\,\phi_1(\xi) \quad \phi_2(\xi) \quad \phi_3(\xi) \quad \phi_4(\xi)\,]^T\mathbf{u}_e \tag{1}$$

where the shape functions are

$$\begin{aligned}\phi_1(\xi) &= 1-3\frac{\xi^2}{l_e^2}+2\frac{\xi^3}{l_e^3}\\ \phi_2(\xi) &= \xi-2\frac{\xi^2}{l_e}+\frac{\xi^3}{l_e^2}\\ \phi_3(\xi) &= 3\frac{\xi^2}{l_e^2}-2\frac{\xi^3}{l_e^3}\\ \phi_4(\xi) &= -\frac{\xi^2}{l_e}+\frac{\xi^3}{l_e^2}\end{aligned}$$

Applying the generalized Hamilton's principle (Junior et al. 2009) for the piezoelectric composite finite element gives

$$\int_{t_1}^{t_2}[\delta(T_e-U_e+V_e)+\delta W]dt = 0 \tag{2}$$

where T_e = total kinetic energy in the element; U_e = total mechanical potential energy in the element; V_e = total electric potential energy in the element; and W = total work done by the external mechanical and electrical forces in the element. These can be respectively written as

$$\begin{aligned}T_e &= \frac{1}{2}\int_0^{l_e} m\left(\frac{\partial u}{\partial t}\right)^2 d\xi\\ U_e &= \frac{1}{2}\int_{V_s} S_1^s T_1^s dV_s + \frac{1}{2}\int_{V_p} S_1^p T_1^p dV_p\\ V_e &= \frac{1}{2}\int_{V_p} E_3 D_3 d\xi\\ W &= \int_0^{l_e} f\cdot u d\xi + \int_0^{l_e}\varphi\cdot Q d\xi\end{aligned} \tag{3}$$

where m = effective mass per unit length of the composite beam; S = strain; T = stress; the superscripts s and p denote piezoelectric and substrate layers, respectively; E = electric field in the y-direction; D = electric displacement; the subscripts 1 and 3 denote the x- and y-directions, respectively; f = nonconservative external mechanical force; φ = electric potential; and Q = electric charge. By using the linear-electroelastic constitutive relation for the piezoelectric material, the following relations can be written:

$$\begin{bmatrix} T \\ D \end{bmatrix} = \begin{bmatrix} Y_p & -e_{31} \\ e_{31} & \varepsilon_{33}^S \end{bmatrix}\begin{bmatrix} S \\ E_3 \end{bmatrix} \tag{4}$$

where Y_p = Young's modulus of the piezoelectric material; e_{31} = piezoelectric constant; and ε_{33}^S = permittivity at constant stress. The expressions of the total mechanical and electric potential energies can be respectively expanded as follows:

$$\begin{aligned}U_e &= \frac{1}{2}\int_0^{l_e} YI\mathbf{u}_e^T\left(\frac{\partial^2\mathbf{\Phi}}{\partial\xi^2}\right)\left(\frac{\partial^2\mathbf{\Phi}}{\partial\xi^2}\right)^T\mathbf{u}_e d\xi\\ &\quad -\frac{1}{2}\int_0^{l_e}\vartheta\left(\frac{\partial^2\mathbf{\Phi}}{\partial\xi^2}\right)v\mathbf{u}_e d\xi\\ V_e &= \frac{1}{2}\int_0^{l_e}\vartheta\left(\frac{\partial^2\mathbf{\Phi}}{\partial\xi^2}\right)v\mathbf{u}_e d\xi + \frac{1}{2}C_p v^2\end{aligned} \tag{5}$$

where $YI = b\{[Y_s(h_b^3-h_a^3)+Y_p(h_c^3-h_b^3)]/3\}$ = effective bending stiffness of the composite beam; $\vartheta = [(e_{31}b)/(2h_p)](h_c^2-h_b^2)$ = coupling term; and v = voltage output across the piezoelectric transducer in the element and $C_p = (\varepsilon_{33}^S b l_e)h_p$ = its clamped capacitance, in which b = width of the composite beam. Substituting T_e, U_e, V_e and W into Eq. (2) yields

$$\begin{aligned}&\int_{t_1}^{t_2}\left[-\int_0^{l_e} m\ddot{\mathbf{u}}_e^T\mathbf{\Phi}\mathbf{\Phi}^T\delta\mathbf{u}_e d\xi - \int_0^{l_e} YI\mathbf{u}_e^T\left(\frac{\partial^2\mathbf{\Phi}}{\partial\xi^2}\right)\left(\frac{\partial^2\mathbf{\Phi}}{\partial\xi^2}\right)^T\delta\mathbf{u}_e d\xi\right.\\ &\quad + \int_0^{l_e}\vartheta\left(\frac{\partial^2\mathbf{\Phi}}{\partial\xi^2}\right)v\delta\mathbf{u}_e d\xi + \int_0^{l_e}\vartheta\left(\frac{\partial^2\mathbf{\Phi}^T}{\partial\xi^2}\right)\mathbf{u}_e\delta v d\xi + C_p v\delta v\\ &\quad \left.+\int_0^{l_e} f\mathbf{\Phi}^T\cdot\delta\mathbf{u}_e d\xi + \int_0^{l_e}\delta\varphi\cdot Q d\xi\right]dt = 0\end{aligned} \tag{6}$$

The element mass matrix $\mathbf{M}_e$, stiffness matrix $\mathbf{K}_e$, electromechanical coupling vector $\mathbf{\theta}_e$ and mechanical nodal force vector $\mathbf{F}_e$ can be expressed as follows:

$$\mathbf{M}_e = \int_0^{l_e} m\mathbf{\Phi}\mathbf{\Phi}^T d\xi = \frac{ml_e}{420}\begin{bmatrix} 156 & 22l_e & 54 & -13l_e \\ 22l_e & 4l_e^2 & 13l_e & -3l_e^2 \\ 54 & 13l_e & 156 & -22l_e \\ -13l_e & -3l_e^2 & -22l_e & 4l_e^2 \end{bmatrix} \tag{7}$$

$$\begin{aligned}\mathbf{K}_e &= \int_0^{l_e} YI\left(\frac{d^2\mathbf{\Phi}}{\partial\xi^2}\right)\left(\frac{d^2\mathbf{\Phi}}{\partial\xi^2}\right)^T d\xi\\ &= \frac{YI}{l_e^3}\begin{bmatrix} 12 & 6l_e & -12 & 6l_e \\ 6l_e & 4l_e^2 & -6l_e & 2l_e^2 \\ -12 & -6l_e & 12 & -6l_e \\ 6l_e & 2l_e^2 & -6l_e & 4l_e^2 \end{bmatrix}\end{aligned} \tag{8}$$

$$\mathbf{\theta}_e = \vartheta\int_0^{l_e}\left(\frac{d^2\mathbf{\Phi}}{d\xi^2}\right)d\xi = \vartheta\begin{bmatrix} 0 \\ -1 \\ 0 \\ 1 \end{bmatrix} \tag{9}$$

$$\mathbf{F}_e = \int_0^{l_e} f(\xi,t)\mathbf{\Phi}d\xi \tag{10}$$

If the mechanical force is uniformly distributed, then

$$\mathbf{F}_e = \int_0^{l_e} f(t)\mathbf{\Phi}d\xi = \frac{f(t)l_e}{2}\begin{bmatrix} 1 \\ \frac{l_e}{6} \\ 1 \\ -\frac{l_e}{6} \end{bmatrix} \tag{11}$$

By assembling the element matrices, the global equations of motion are obtained

Downloaded from ascelibrary.org by Hong Kong University of Science and Technology (Guangzhou) on 08/02/24. Copyright ASCE. For personal use only; all rights reserved.

$$\mathbf{M}\ddot{\mathbf{u}} + \mathbf{C}\dot{\mathbf{u}} + \mathbf{K}\mathbf{u} - \mathbf{\Theta}\mathbf{v} = \mathbf{F}$$
$$\mathbf{C}_p\mathbf{v} + \mathbf{Q} + \mathbf{\Theta}^T\mathbf{u} = 0 \tag{12}$$

In the most general case, each piezoelectric element has its own independent electrode pair; $\mathbf{v}$ is a $n_e \times 1$ vector and $\mathbf{\Theta}$ is a $(2n_e + 2) \times n_e$ matrix, where n_e is the number of elements to be used for meshing the beam. In practical applications, the voltage degrees of freedom on the top and bottom surfaces of the beam are coupled by conductive electrode layers to provide uniform electric potentials. Therefore, all piezoelectric composite finite elements should provide the same voltage output and all the elements in vector $\mathbf{v}$ should be identical

$$\mathbf{v} = [\, v_1 \quad v_2 \quad \ldots \quad v_{n_e}\,]^T = [\,1 \quad 1 \quad \ldots \quad 1\,]^T v_p \tag{13}$$

The voltage output v_p is a scalar which represents the uniform electric potential. By redefining the electromechanical coupling vector $\tilde{\mathbf{\Theta}} = \mathbf{\Theta}[\,1 \quad 1 \quad \ldots \quad 1\,]^T$ [$\tilde{\mathbf{\Theta}}$ becomes a $(2n_e + 2) \times 1$ vector], the governing equations are rewritten as

$$\mathbf{M}\ddot{\mathbf{u}} + \mathbf{C}\dot{\mathbf{u}} + \mathbf{K}\mathbf{u} - \tilde{\mathbf{\Theta}}v_p = \mathbf{F}$$
$$n_e C_p \dot{v}_p + \frac{v_p}{R} + \tilde{\mathbf{\Theta}}^T\dot{\mathbf{u}} = 0 \tag{14}$$

Infinitely Long Metamaterial Beam

This section analyzes the band structures of the metamaterial beam and the phononic metamaterial beam using the proposed method based on the derived 1D two-node piezoelectric composite finite element.

Band Structure of Metamaterial Beam

Fig. 2 shows the infinitely long model of a metamaterial beam. Uniform local resonators are periodically attached onto the host plain beam at a constant separation distance l. Each resonator consists of a mass of m_1 and a spring with a linear stiffness of k_1. By using the conventional 1D two-node beam element (omitting the electrical DOF in the developed piezoelectric composite finite element), this infinitely long model can be discretized [Fig. 3(a)]. Different shaded areas denote different cells. Each cell is assumed to be meshed with $(n - 1)$ elements. Therefore, each beam section consists of n nodes and each cell consists of $n + 1$ nodes, of which the additional node represents the attached local resonator. It is assumed that the different shaded areas in Fig. 3 denote the $(j - 1)$th, jth, and $(j + 1)$th cells, respectively. By adopting Bloch's theorem, the transverse displacement amplitude vectors for nodes in the three shaded areas can be written as $[A_1 \quad A_2 \quad \ldots \quad A_n \quad C]^T e^{-iql}$, $[A_1 \quad A_2 \quad \ldots \quad A_n \quad C]^T$ and $[A_1 \quad A_2 \quad \ldots \quad A_n \quad C]^T e^{iql}$, respectively, where $A_1, A_2, \ldots, A_n$ denote the transverse displacement amplitudes of n nodes in the beam section in the unit cell, and C denotes the displacement amplitude of the local resonator. The global mass and stiffness matrices of this infinitely long system can be constructed. For example, the global mass matrix after construction is in the form shown in Fig. 3(b), in which a small square represents a 2×2 submatrix and a large square represents a 4×4 submatrix. All other elements outside the small/large squares are zeros. The global matrices are periodically repeating. The following procedure is proposed to obtain the dispersion relation. First, the repeating pattern from the whole matrices considering only three neighboring cells is extracted. The repeating mass and stiffness matrices are of size $(6n + 3) \times (6n + 3)$. Each row represents an equation [Fig. 3(b)]. The lines denote either nodal translation DOF–related equations or nodal rotation DOF–related equations, and the oval denotes the resonator-related equation. Because there are only $2n + 1$ unique independent DOFs of $n + 1$ nodes, i.e., others are periodically repeated, there are only $2n + 1$ unique independent equations. To extract the $2n + 1$ featured fundamental equations, extract the first n nodal translation DOF–related equations from top to bottom, the last n nodal rotation DOF–related equations from bottom to top [Fig. 3(a)], and the intermediate resonator-related equation. By writing the $2n + 1$ equations in matrix form, the coefficient matrix should be of the size $(2n + 1) \times (2n + 1)$. Then, by equating the determinant of the $(2n + 1) \times (2n + 1)$ matrix to zero to verify the existence of nontrivial solutions, the dispersion relation of the system can be derived.

Although each cell theoretically can be meshed with any positive integer number of elements, in practice, upon the achievement of convergence, the optimum number of elements should be used to balance accuracy and computational cost. Taking the simplest case as an example, i.e., the case in which each cell is meshed with a single element, the global mass and stiffness matrices of this system can be constructed as Eqs. (15) and (16), respectively

$$\begin{bmatrix}
\cdots & & & & & & & & & & \\
 & \frac{156ml_e}{420}+\frac{156ml_e}{420} & -\frac{22ml_e^2}{420}+\frac{22ml_e^2}{420} & 0 & \frac{54ml_e}{420} & -\frac{13ml_e^2}{420} & & & & & \\
 & -\frac{22ml_e^2}{420}+\frac{22ml_e^2}{420} & \frac{4ml_e^3}{420}+\frac{4ml_e^3}{420} & 0 & \frac{13ml_e^2}{420} & -\frac{3ml_e^3}{420} & & & & & \\
 & 0 & 0 & m_1 & 0 & 0 & & & & & \\
 & \frac{54ml_e}{420} & \frac{13ml_e^2}{420} & 0 & \frac{156ml_e}{420}+\frac{156ml_e}{420} & -\frac{22ml_e^2}{420}+\frac{22ml_e^2}{420} & 0 & \frac{54ml_e}{420} & -\frac{13ml_e^2}{420} & & \\
 & -\frac{13ml_e^2}{420} & -\frac{3ml_e^3}{420} & 0 & -\frac{22ml_e^2}{420}+\frac{22ml_e^2}{420} & \frac{4ml_e^3}{420}+\frac{4ml_e^3}{420} & 0 & \frac{13ml_e^2}{420} & -\frac{3ml_e^3}{420} & & \\
 & & & & 0 & 0 & m_1 & 0 & 0 & & \\
 & & & & \frac{54ml_e}{420} & \frac{13ml_e^2}{420} & 0 & \frac{156ml_e}{420} & -\frac{22ml_e^2}{420} & 0 & \\
 & & & & -\frac{13ml_e^2}{420} & -\frac{3ml_e^3}{420} & 0 & -\frac{22ml_e^2}{420} & \frac{4ml_e^3}{420} & 0 & \\
 & & & & & & & 0 & 0 & m_1 & \\
 & & & & & & & & & & \cdots
\end{bmatrix} \tag{15}$$

J. Aerosp. Eng., 2018, 31(6): 04018088

Downloaded from ascelibrary.org by Hong Kong University of Science and Technology (Guangzhou) on 08/02/24. Copyright ASCE. For personal use only; all rights reserved.

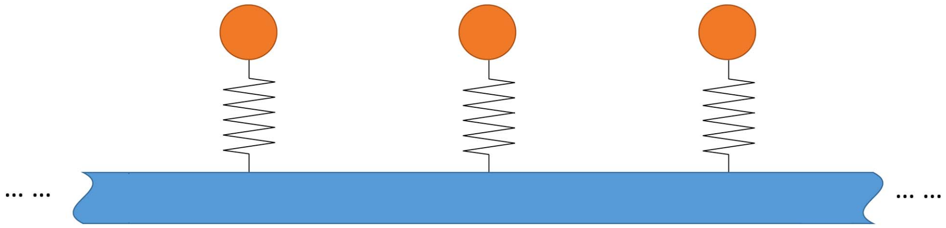

Fig. 2. Infinitely long model of metamaterial beam.

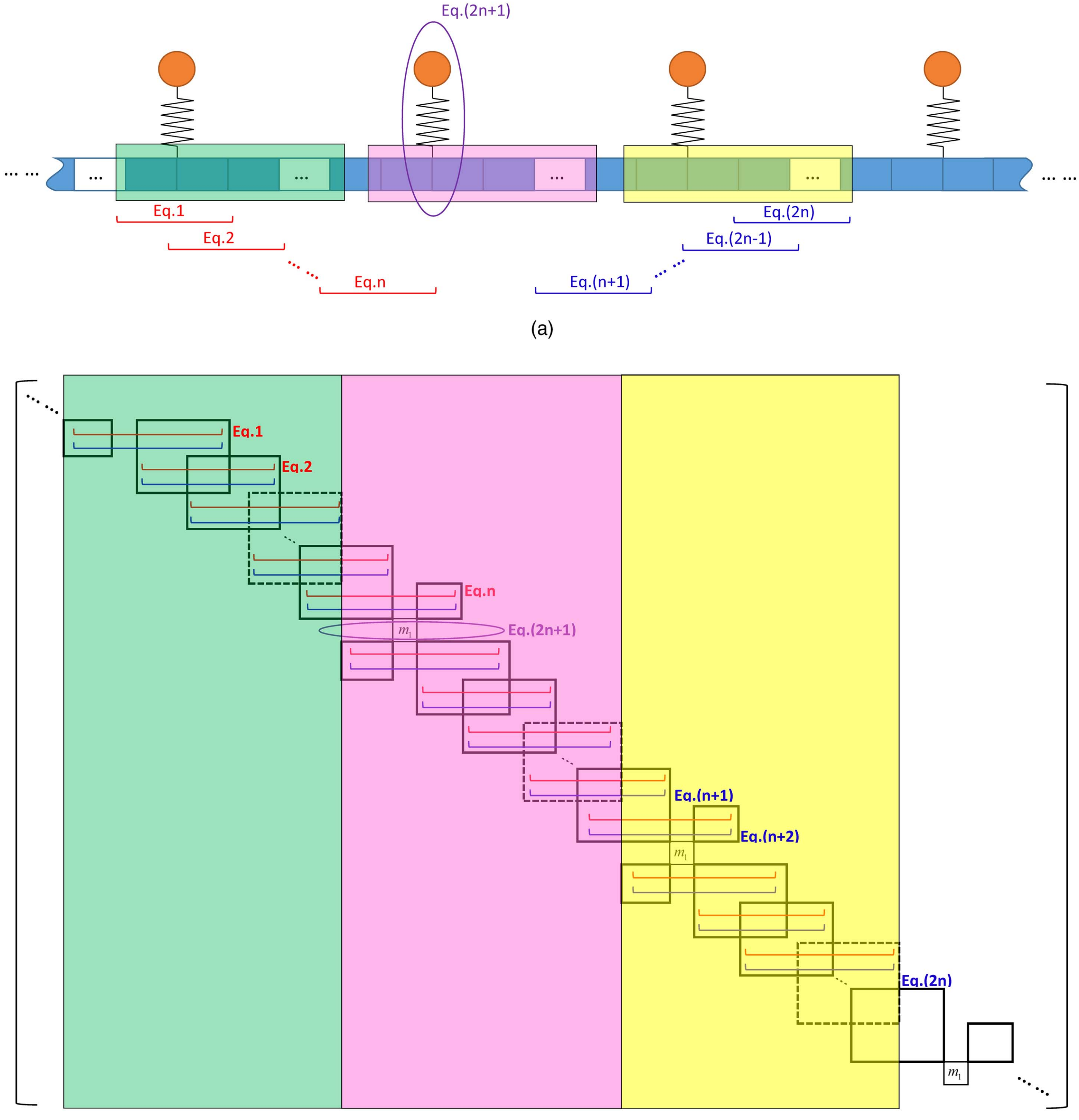

Fig. 3. (a) Discretized metamaterial beam; and (b) general form of global mass matrix of discretized metamaterial beam.

Downloaded from ascelibrary.org by Hong Kong University of Science and Technology (Guangzhou) on 08/02/24. Copyright ASCE. For personal use only; all rights reserved.

Downloaded from ascelibrary.org by Hong Kong University of Science and Technology (Guangzhou) on 08/02/24. Copyright ASCE. For personal use only; all rights reserved.

$$\begin{bmatrix} \cdots & & & & & & & & & \\ & 12\frac{YI}{l_e^3}+k_1+12\frac{YI}{l_e^3} & -6\frac{YI}{l_e^2}+6\frac{YI}{l_e^2} & -k_1 & -12\frac{YI}{l_e^3} & 6\frac{YI}{l_e^2} & & & & \\ & -6\frac{YI}{l_e^2}+6\frac{YI}{l_e^2} & 4\frac{YI}{l_e}+4\frac{YI}{l_e} & 0 & -6\frac{YI}{l_e^2} & 2\frac{YI}{l_e} & & & & \\ & -k_1 & 0 & k_1 & 0 & 0 & & & & \\ & -12\frac{YI}{l_e^3} & -6\frac{YI}{l_e^2} & 0 & 12\frac{YI}{l_e^3}+k_1+12\frac{YI}{l_e^3} & -6\frac{YI}{l_e^2}+6\frac{YI}{l_e^2} & -k_1 & -12\frac{YI}{l_e^3} & 6\frac{YI}{l_e^2} & \\ & 6\frac{YI}{l_e^2} & 2\frac{YI}{l_e} & 0 & -6\frac{YI}{l_e^2}+6\frac{YI}{l_e^2} & 4\frac{YI}{l_e}+4\frac{YI}{l_e} & 0 & -6\frac{YI}{l_e^2} & 2\frac{YI}{l_e} & \\ & & & & -k_1 & 0 & k_1 & 0 & 0 & \\ & & & & -12\frac{YI}{l_e^3} & -6\frac{YI}{l_e^2} & 0 & 12\frac{YI}{l_e^3}+k_1 & -6\frac{YI}{l_e^2} & -k_1 \\ & & & & 6\frac{YI}{l_e^2} & 2\frac{YI}{l_e} & 0 & -6\frac{YI}{l_e^2} & 4\frac{YI}{l_e} & 0 \\ & & & & & & & -k_1 & 0 & k_1 \\ & & & & & & & & & \cdots \end{bmatrix} \tag{16}$$

The system is assumed to be infinitely long. Thus, the mass and stiffness matrices are correspondingly in a periodic repeating pattern. Based on Bloch's theorem, the nodal displacements are assumed to be in the following forms:

$$\begin{aligned} w_j(t) &= Ae^{i(qx-\omega t)} \\ \theta_j(t) &= Be^{i(qx-\omega t)} \\ u_j(t) &= Ce^{i(qx-\omega t)} \end{aligned} \tag{17}$$

where i = imaginary unit; and q = wave number. The repeating patterns of the mass and stiffness matrices are

$$\widehat{\mathbf{M}} = \begin{bmatrix} \frac{54ml_e}{420} & \frac{13ml_e^2}{420} & 0 & \frac{156ml_e}{420}+\frac{156ml_e}{420} & -\frac{22ml_e^2}{420}+\frac{22ml_e^2}{420} & 0 & \frac{54ml_e}{420} & -\frac{13ml_e^2}{420} & 0 \\ -\frac{13ml_e^2}{420} & -\frac{3ml_e^3}{420} & 0 & -\frac{22ml_e^2}{420}+\frac{22ml_e^2}{420} & \frac{4ml_e^3}{420}+\frac{4ml_e^3}{420} & 0 & \frac{13ml_e^2}{420} & -\frac{3ml_e^3}{420} & 0 \\ 0 & 0 & 0 & 0 & 0 & m_1 & 0 & 0 & 0 \end{bmatrix} \tag{18}$$

$$\widehat{\mathbf{K}} = \begin{bmatrix} -12\frac{YI}{l_e^3} & -6\frac{YI}{l_e^2} & 0 & 12\frac{YI}{l_e^3}+k_1+12\frac{YI}{l_e^3} & -6\frac{YI}{l_e^2}+6\frac{YI}{l_e^2} & -k_1 & -12\frac{YI}{l_e^3} & 6\frac{YI}{l_e^2} & 0 \\ 6\frac{YI}{l_e^2} & 2\frac{YI}{l_e} & 0 & -6\frac{YI}{l_e^2}+6\frac{YI}{l_e^2} & 4\frac{YI}{l_e}+4\frac{YI}{l_e} & 0 & -6\frac{YI}{l_e^2} & 2\frac{YI}{l_e} & 0 \\ 0 & 0 & 0 & -k_1 & 0 & k_1 & 0 & 0 & 0 \end{bmatrix} \tag{19}$$

The governing equation for the repeating pattern of the system is written as

$$\widehat{\mathbf{M}}\,\ddot{\mathbf{u}} + \widehat{\mathbf{K}}\mathbf{u} = 0 \tag{20}$$

Substituting Eqs. (17) into (20) yields

$$\left\{ -\omega^2 \begin{bmatrix} \frac{54ml_e}{420}e^{-iql} + \left(\frac{156ml_e}{420}+\frac{156ml_e}{420}\right) + \frac{54ml_e}{420}e^{iql} & \frac{13ml_e^2}{420}e^{-iql} + \left(-\frac{22ml_e^2}{420}+\frac{22ml_e^2}{420}\right) - \frac{13ml_e^2}{420}e^{iql} & 0 \\ -\frac{13ml_e^2}{420}e^{-iql} + \left(-\frac{22ml_e^2}{420}+\frac{22ml_e^2}{420}\right) + \frac{13ml_e^2}{420}e^{iql} & -\frac{3ml_e^3}{420}e^{-iql} + \left(\frac{4ml_e^3}{420}+\frac{4ml_e^3}{420}\right) - \frac{3ml_e^3}{420}e^{iql} & 0 \\ 0 & 0 & m_1 \end{bmatrix} \right.$$

$$\left. + \begin{bmatrix} -12\frac{YI}{l_e^3}e^{-iql} + \left(12\frac{YI}{l_e^3}+k_1+12\frac{YI}{l_e^3}\right) - 12\frac{YI}{l_e^3}e^{iql} & -6\frac{YI}{l_e^2}e^{-iql} + \left(-6\frac{YI}{l_e^2}+6\frac{YI}{l_e^2}\right) + 6\frac{YI}{l_e^2}e^{iql} & -k_1 \\ 6\frac{YI}{l_e^2}e^{-iql} + \left(-6\frac{YI}{l_e^2}+6\frac{YI}{l_e^2}\right) - 6\frac{YI}{l_e^2}e^{iql} & 2\frac{YI}{l_e}e^{-iql} + \left(4\frac{YI}{l_e}+4\frac{YI}{l_e}\right) + 2\frac{YI}{l_e}e^{iql} & 0 \\ -k_1 & 0 & k_1 \end{bmatrix} \right\} \cdot \begin{bmatrix} A \\ B \\ C \end{bmatrix} = 0 \tag{21}$$

The repeating patterns of the mass and stiffness matrices are of size 3 × 6. However, after substituting them into Eq. (20) and rearranging, because of the assumption of periodicity and the implementation of Bloch's theorem [Eq. (17)], they are degraded into 3 × 3 matrices [Eq. (21)]. In order to guarantee the existence of a nontrivial solution of Eq. (21), the determinant of the coefficient matrix of Eq. (21) has to be zero, which leads to the following dispersion equation:

$$\begin{vmatrix} 24\frac{YI}{l_e^3}(1-\cos ql)+k_1-\omega^2\left(\frac{54ml_e}{210}\cos ql+\frac{156ml_e}{210}\right) & i\left(12\frac{YI}{l_e^2}\sin ql+\omega^2\frac{13ml_e^2}{210}\sin ql\right) & -k_1 \\ i\left(-12\frac{YI}{l_e^2}\sin ql-\omega^2\frac{13ml_e^2}{210}\sin ql\right) & (2+\cos ql)\left(4\frac{YI}{l_e}\right)-\omega^2\left(-\frac{3ml_e^3}{210}\cos ql+\frac{4ml_e^3}{210}\right) & 0 \\ -k_1 & 0 & k_1-\omega^2 m_1 \end{vmatrix}=0 \quad (22)$$

Fig. 4(a) shows the band structure of the system being studied. Table 1 lists the geometry and material properties of the host beam and the resonator parameters. Unless explicitly stated otherwise, the following sections use the same parameters for the host beam and resonators in all the models. The result calculated by using the transfer matrix method is also provided for comparison. In the low-frequency range, the proposed method well predicts the existence and the location of the band gap. However, for the coarse mesh case, i.e., the case in which each section is meshed with a single element, as the frequency increases, the result from the proposed method deviates significantly from that of the TMM method due to the lack of sufficient mesh resolution. Increasing the number of elements for each cell produces results from the proposed method that converge to those from the TMM method [Fig. 4(b)]. By meshing each cell with four elements, the band gap predicted by the proposed method is 97.71–143.28 Hz, which is sufficiently accurate compared with the result from TMM (97.71–143.30 Hz). In addition, for the TMM method, the band structure should be obtained by sweeping over ω and solving for q. In the proposed method, the procedure is the reverse: the band structure is obtained by sweeping q and solving for ω. The TMM method involves beam equations that consist of trigonometric functions and hyperbolic functions. The transfer matrix is thus often relatively complex, and the derived dispersion equation is relatively difficult to solve. However, in the proposed method, the obtained dispersion equation [Eq. (22)] is in a much simpler form, leading to higher computational efficiency.

Band Structure of Phononic Metamaterial Beam

This section investigates the infinitely long model of a piezoelectric metamaterial beam (Fig. 5). The piezoelectric transducers are periodically bonded onto the bottom surface of the host beam. The impedance mismatch between the subsections with and without the piezoelectric coverage produces Bragg scattering, which forms the Bragg scattering–type band gap in this beam. Because this

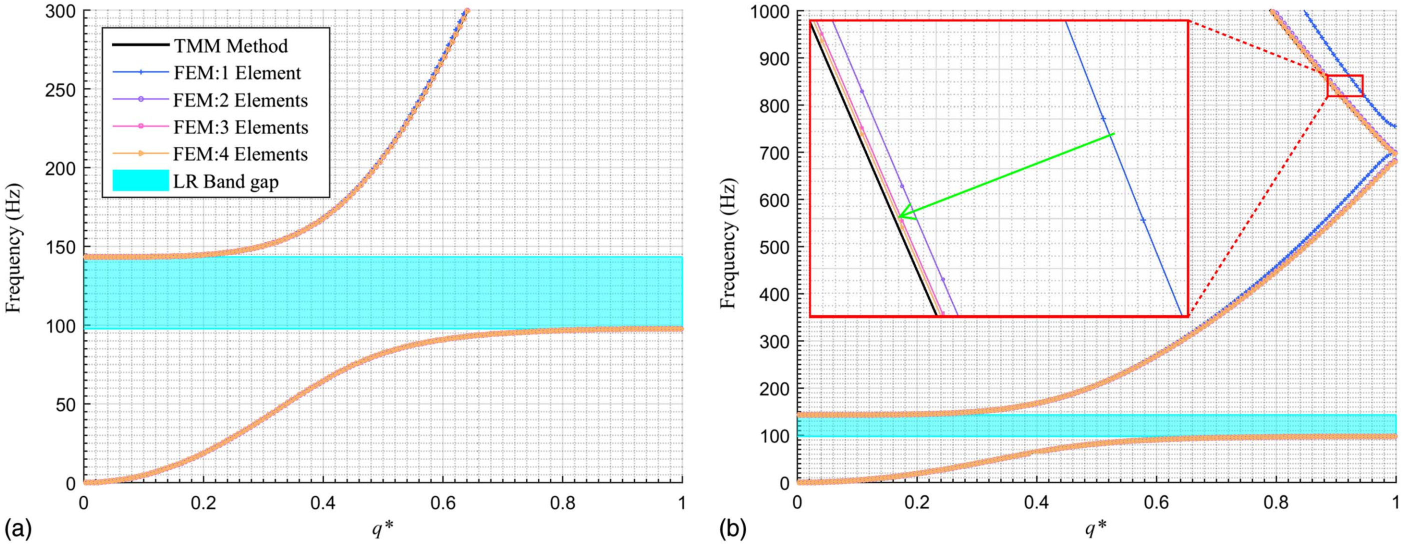

Fig. 4. (a) Band structures of metamaterial beam from proposed method and TMM method; and (b) close-up view to demonstrate convergence.

Table 1. Geometry and material properties of host beam and resonators

Parameter	Value
Host beam mass density	1,180 kg/m^3
Host beam Young's modulus	4.35 GPa
Host beam width	0.02 m
Host beam thickness	0.005 m
Local resonator mass	0.01 kg
Local resonator spring stiffness	3,947.8 N/m
Lattice constant	0.08 m

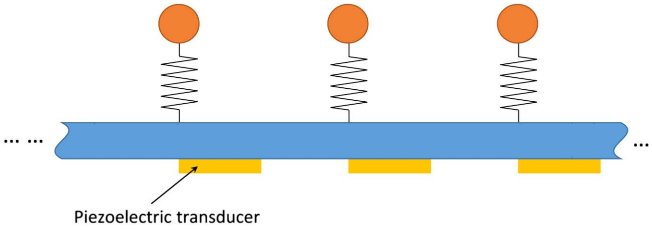

Fig. 5. Infinitely long model of phononic metamaterial beam.

Downloaded from ascelibrary.org by Hong Kong University of Science and Technology (Guangzhou) on 08/02/24. Copyright ASCE. For personal use only; all rights reserved.

piezoelectric metamaterial beam possesses both Bragg gap and LR gap, therefore, it is referred to as a phononic metamaterial beam. The governing equations of the phononic metamaterial beam are

$$\begin{gathered}\mathbf{M}\ddot{\mathbf{u}} + \mathbf{K}\mathbf{u} - \tilde{\boldsymbol{\Theta}}\mathbf{v}_p = 0 \\ n_e C_p \dot{\mathbf{v}}_p + \frac{\mathbf{v}_p}{R} + \tilde{\boldsymbol{\Theta}}^T \dot{\mathbf{u}} = 0\end{gathered} \tag{23}$$

Short-Circuit Condition

This subsection assumes the piezoelectric transducers to be under short-circuit condition. Therefore all the elements in the voltage vector $\mathbf{v}_p$ are set to zero. This section demonstrates the calculation procedure for the simplest case, i.e., each subsection is meshed with a single element and each cell is meshed with two elements. First, the global mass and stiffness matrices of this system can be constructed as Eqs. (24) and (25), respectively

$$\begin{bmatrix} \cdots & & & & & & & & & \\ \frac{54m_al_a}{420} & \frac{13m_al_a^2}{420} & 0 & \frac{156m_al_a}{420}+\frac{156m_bl_b}{420} & -\frac{22m_al_a^2}{420}+\frac{22m_bl_b^2}{420} & \frac{54m_bl_b}{420} & -\frac{13m_bl_b^2}{420} & & & \\ -\frac{13m_al_a^2}{420} & -\frac{3m_al_a^3}{420} & 0 & -\frac{22m_al_a^2}{420}+\frac{22m_bl_b^2}{420} & \frac{4m_al_a^3}{420}+\frac{4m_bl_b^3}{420} & \frac{13m_bl_b^2}{420} & -\frac{3m_bl_b^3}{420} & & & \\ & & & \frac{54m_bl_b}{420} & \frac{13m_bl_b^2}{420} & \frac{156m_bl_b}{420}+\frac{156m_al_a}{420} & -\frac{22m_bl_b^2}{420}+\frac{22m_al_a^2}{420} & 0 & \frac{54m_al_a^2}{420} & -\frac{13m_al_a^2}{420} \\ & & & -\frac{13m_bl_b^2}{420} & -\frac{3m_bl_b^3}{420} & -\frac{22m_bl_b^2}{420}+\frac{22m_al_a^2}{420} & \frac{4m_bl_b^3}{420}+\frac{4m_al_a^3}{420} & 0 & \frac{13m_al_a^2}{420} & -\frac{3m_al_a^3}{420} \\ & & & & & & & m_1 & & \\ & & & & & & & & & \cdots \end{bmatrix} \tag{24}$$

$$\begin{bmatrix} \cdots & & & & & & & & & \\ -\frac{12Y_aI_a}{l_a^3} & -\frac{6Y_aI_a}{l_a^2} & 0 & \frac{12Y_aI_a}{l_a^3}+\frac{12Y_bI_b}{l_b^3} & -\frac{6Y_aI_a}{l_a^2}+\frac{6Y_bI_b}{l_b^2} & -\frac{12Y_bI_b}{l_b^3} & \frac{6Y_bI_b}{l_b^2} & & & \\ \frac{6Y_aI_a}{l_a^2} & \frac{2Y_aI_a}{l_a} & 0 & -\frac{6Y_aI_a}{l_a^2}+\frac{6Y_bI_b}{l_b^2} & \frac{4Y_aI_a}{l_a}+\frac{4Y_bI_b}{l_b} & -\frac{6Y_bI_b}{l_b^2} & \frac{2Y_bI_b}{l_b} & & & \\ & & & -\frac{12Y_bI_b}{l_b^3} & -\frac{6Y_bI_b}{l_b^2} & \frac{12Y_bI_b}{l_b^3}+k_1+\frac{12Y_aI_a}{l_a^3} & -\frac{6Y_bI_b}{l_b^2}+\frac{6Y_aI_a}{l_a^2} & -k_1 & -\frac{12Y_aI_a}{l_a^3} & \frac{6Y_aI_a}{l_a^2} \\ & & & \frac{6Y_bI_b}{l_b^2} & \frac{2Y_bI_b}{l_b} & -\frac{6Y_bI_b}{l_b^2}+\frac{6Y_aI_a}{l_a^2} & \frac{4Y_bI_b}{l_b}+\frac{4Y_aI_a}{l_a} & 0 & -\frac{6Y_aI_a}{l_a^2} & \frac{2Y_aI_a}{l_a} \\ & & & & & -k_1 & & k_1 & & \\ & & & & & & & & & \cdots \end{bmatrix} \tag{25}$$

in which the subscripts a and b denote the subsections with and without piezoelectric coverage, respectively; l_a and l_b = lengths of the elements within the subsections with and without piezoelectric coverage, respectively; and l = lattice constant. By following the same procedure presented in the previous section, the repeating patterns of the mass and stiffness matrices are extracted and the dispersion relation of this phononic metamaterial beam is obtained as

$$|-\omega^2\mathbf{M} + \mathbf{K}| = 0 \tag{26}$$

in which

$$\mathbf{M} = \begin{bmatrix} \left(\frac{54m_al_a}{420}e^{-iql}+\frac{54m_bl_b}{420}\right) & \left(\frac{13m_al_a^2}{420}e^{-iql}-\frac{13m_bl_b^2}{420}\right) & \left(\frac{156m_al_a}{420}+\frac{156m_bl_b}{420}\right)e^{-iql} & \left(-\frac{22m_al_a^2}{420}+\frac{22m_bl_b^2}{420}\right)e^{-iql} & 0 \\ \left(\frac{156m_bl_b}{420}+\frac{156m_al_a}{420}\right) & \left(-\frac{22m_bl_b^2}{420}+\frac{22m_al_a^2}{420}\right) & \left(\frac{54m_bl_b}{420}e^{-iql}+\frac{54m_al_a^2}{420}\right) & \left(\frac{13m_bl_b^2}{420}e^{-iql}-\frac{13m_al_a^2}{420}\right) & 0 \\ \left(-\frac{13m_al_a^2}{420}+\frac{13m_bl_b^2}{420}e^{iql}\right) & \left(-\frac{3m_al_a^3}{420}-\frac{3m_bl_b^3}{420}e^{iql}\right) & \left(-\frac{22m_al_a^2}{420}+\frac{22m_bl_b^2}{420}\right) & \left(\frac{4m_al_a^3}{420}+\frac{4m_bl_b^3}{420}\right) & 0 \\ \left(-\frac{22m_bl_b^2}{420}+\frac{22m_al_a^2}{420}\right)e^{iql} & \left(\frac{4m_bl_b^3}{420}+\frac{4m_al_a^3}{420}\right)e^{iql} & \left(-\frac{13m_bl_b^2}{420}+\frac{13m_al_a^2}{420}e^{iql}\right) & \left(-\frac{3m_bl_b^3}{420}-\frac{3m_al_a^3}{420}e^{iql}\right) & 0 \\ 0 & 0 & 0 & 0 & m_1 \end{bmatrix} \tag{27}$$

Downloaded from ascelibrary.org by Hong Kong University of Science and Technology (Guangzhou) on 08/02/24. Copyright ASCE. For personal use only; all rights reserved.

$$\mathbf{K}=\begin{bmatrix} \left(-\frac{12Y_aI_a}{l_a^3}e^{-iql}-\frac{12Y_bI_b}{l_b^3}\right) & \left(-\frac{6Y_aI_a}{l_a^2}e^{-iql}+\frac{6Y_bI_b}{l_b^2}\right) & \left(\frac{12Y_aI_a}{l_a^3}+\frac{12Y_bI_b}{l_b^3}\right)e^{-iql} & \left(-\frac{6Y_aI_a}{l_a^2}+\frac{6Y_bI_b}{l_b^2}\right)e^{-iql} & 0 \\ \left(\frac{12Y_bI_b}{l_b^3}+k_1+\frac{12Y_aI_a}{l_a^3}\right) & \left(-\frac{6Y_bI_b}{l_b^2}+\frac{6Y_aI_a}{l_a^2}\right) & \left(-\frac{12Y_bI_b}{l_b^3}e^{-iql}-\frac{12Y_aI_a}{l_a^3}\right) & \left(-\frac{6Y_bI_b}{l_b^2}e^{-iql}+\frac{6Y_aI_a}{l_a^2}\right) & -k_1 \\ \left(\frac{6Y_aI_a}{l_a^2}-\frac{6Y_bI_b}{l_b^2}e^{iql}\right) & \left(\frac{2Y_aI_a}{l_a}+\frac{2Y_bI_b}{l_b}e^{iql}\right) & \left(-\frac{6Y_aI_a}{l_a^2}+\frac{6Y_bI_b}{l_b^2}\right) & \left(\frac{4Y_aI_a}{l_a}+\frac{4Y_bI_b}{l_b}\right) & 0 \\ \left(-\frac{6Y_bI_b}{l_b^2}+\frac{6Y_aI_a}{l_a^2}\right)e^{iql} & \left(\frac{4Y_bI_b}{l_b}+\frac{4Y_aI_a}{l_a}\right)e^{iql} & \left(\frac{6Y_bI_b}{l_b^2}-\frac{6Y_aI_a}{l_a^2}e^{iql}\right) & \left(\frac{2Y_bI_b}{l_b}+\frac{2Y_aI_a}{l_a}e^{iql}\right) & 0 \\ -k_1 & 0 & 0 & 0 & k_1 \end{bmatrix} \tag{28}$$

Fig. 6 shows the band structure of the phononic metamaterial beam. Table 2 lists the geometric and material parameters of the piezoelectric transducers (PZT-5H). To maintain consistency, the same type of piezoelectric transducer was used in all the models under investigation throughout this paper.

The result from the proposed method is in good agreement with that from the TMM method. The LR gap predicted by the proposed method and the TMM method are almost identical, 98.31–139.12 Hz and 98.31–139.13 Hz, respectively. Over the frequency range 0–1,000 Hz, compared with the metamaterial beam without any piezoelectric coverage, the phononic metamaterial beam can provide an additional Bragg band gap which is generated by the periodic impedance mismatch between the subsections with and without piezoelectric coverage. The Bragg gap predicted by the proposed method and the TMM method are very close, 707.84–834.80 Hz and 707.67–834.51 Hz, respectively.

Open-Circuit Condition

This case assumed the piezoelectric transducers to be under open-circuit condition. Eliminating the voltage vector $\mathbf{v}_p$ in Eq. (23) obtains

$$\mathbf{M}\ddot{\mathbf{u}}+\underbrace{\left(\mathbf{K}+\frac{\tilde{\mathbf{\Theta}}\tilde{\mathbf{\Theta}}^T}{n_eC_p}\right)}_{\mathbf{K}_{eff}}\mathbf{u}=0 \tag{29}$$

where the electromechanical coupling induces an increase in the stiffness of the system. For the case of each subsection meshed with a single element, $\tilde{\mathbf{\Theta}}\tilde{\mathbf{\Theta}}^T$ can be calculated as follows:

$$\tilde{\mathbf{\Theta}}\tilde{\mathbf{\Theta}}^T=\begin{bmatrix} 0 & 0 & 0 & 0 & 0 \\ 0 & 0 & 0 & 0 & 0 \\ 0 & -\theta^2 & 0 & \theta^2 & 0 \\ 0 & \theta^2e^{iql} & 0 & -\theta^2e^{iql} & 0 \\ 0 & 0 & 0 & 0 & 0 \end{bmatrix} \tag{30}$$

By integrating the electromechanical coupling–related matrix with the mechanical stiffness matrix and then applying the same procedure, the dispersion relation of the phononic metamaterial beam under open-circuit condition can be derived. For the previously investigated phononic metamaterial beam, Fig. 7 shows its band structure under open-circuit condition.

The LR gap is almost unaffected irrespective of whether the piezoelectric transducers are under short-circuit condition (98.31–139.12 Hz) or open-circuit condition (98.33–139.12 Hz) [Fig. 7(a)]. This is expected because the local resonant gap only depends on the properties of local resonators, and the shift between short-circuit and open-circuit conditions of the piezoelectric transducers does not influence the local resonators. The width of the Bragg gap increases when piezoelectric transducers are under open-circuit condition (708.03–848.70 Hz) compared with that under short-circuit condition (707.84–834.80 Hz). This is because when piezoelectric transducers are under open-circuit condition, the piezoelectric effect stiffens the beam and resists the beam deformation. Consequently, the impedance mismatch between the subsections with and without piezoelectric coverage becomes more significant, leading to a larger Bragg gap (Lu et al. 2009). The existing TMM method

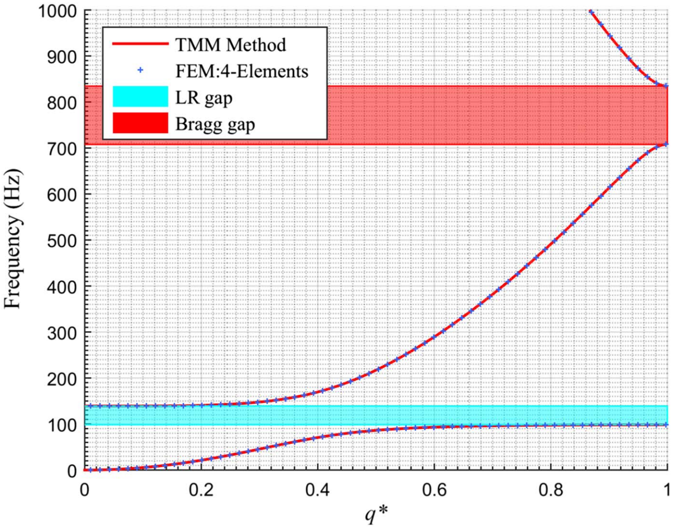

Fig. 6. Comparison of band structures of phononic metamaterial beam under short-circuit condition from proposed method and TMM method.

Table 2. Geometric and material properties of PZT-5H

Parameter	Value
PZT-5H mass density	7,500 kg/m^3
s_{11}^E	1.65×10^{-11} m^3/N
d_{31}	-2.74×10^{-10} m/V
e_{31}	-16.6 C/m^2
ε_{33}^T	3.01×10^{-8} F/m
PZT-5H width	0.02 m
PZT-5H length	0.04 m
PZT-5H thickness	0.0002 m

Downloaded from ascelibrary.org by Hong Kong University of Science and Technology (Guangzhou) on 08/02/24. Copyright ASCE. For personal use only; all rights reserved.

Downloaded from ascelibrary.org by Hong Kong University of Science and Technology (Guangzhou) on 08/02/24. Copyright ASCE. For personal use only; all rights reserved.

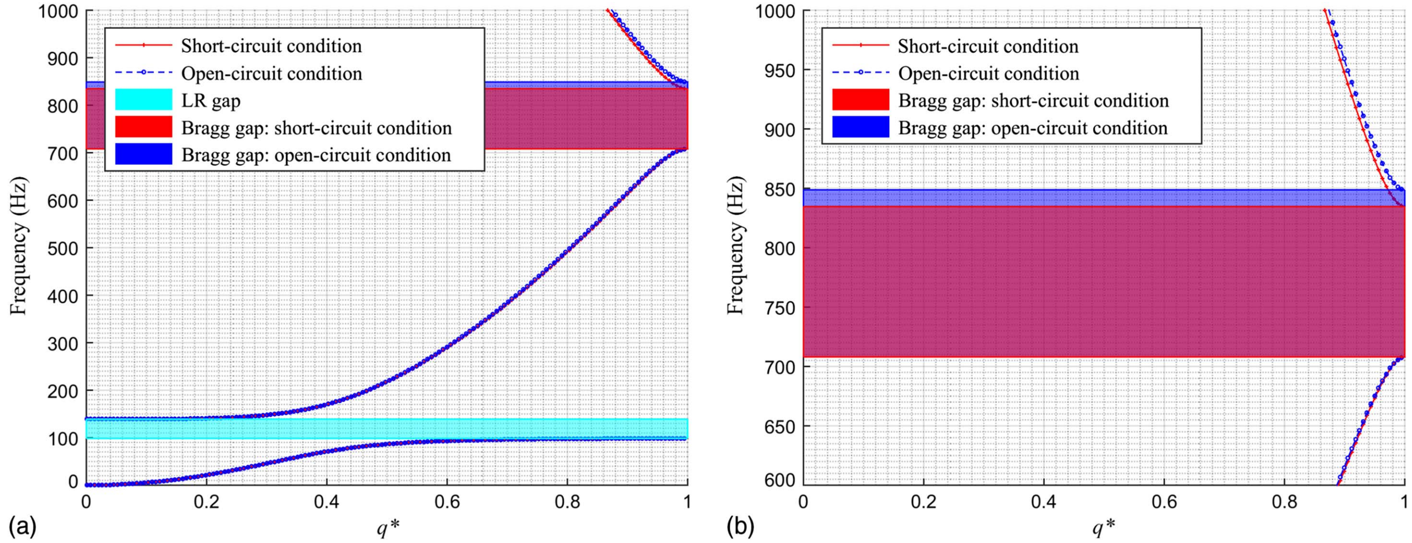

Fig. 7. (a) Band structures of phononic metamaterial beam with piezoelectric transducers under short-circuit and open-circuit conditions; and (b) close-up view of Bragg gap.

cannot consider the piezoelectric effect. Hence, this paper does not provide the TMM-calculated band structure result for open-circuit condition for comparison. The following section verifies the band gaps from the band structure for the infinitely long model of the phononic metamaterial beam under open-circuit condition by comparing it with the transmittance of the finitely long counterpart model.

Finitely Long Metamaterial Beam

This section evaluates two more practical finitely long models of a metamaterial beam with certain energy dissipation mechanisms.

Transmittance of Metamaterial Beam

Fig. 8 shows the finitely long model of the metamaterial beam. Bonding a piezoelectric transducer at the clamped end of the beam fortuitously imparts the system with energy harvesting functionality in addition to the intrinsic vibration suppression.

With the parameters listed in Tables 1 and 2 and assuming a host beam length of 0.12 m (thus incorporating three resonators attached onto the host beam), Fig. 9 shows the transmittances of the metamaterial beam with the piezoelectric transducer under short-circuit and open-circuit conditions. Classical Rayleigh damping is applied to the host beam. The mass-proportional damping coefficient and the stiffness-proportional damping coefficient are assigned to make both the damping ratios for the first and the second modes equal to 0.09. The damping ratio of the resonator used in the calculation is also set to be 0.09. The piezoelectric-covered composite subsection is meshed with four elements. Each of other cells without piezoelectric coverage is also meshed with four elements. The results from the FE solution obtained from ANSYS are provided for comparison. For the model developed with ANSYS, the host beam is modeled with three-dimensional (3D) 20-node structural solid elements (SOLID186), and the piezoelectric transducers are modelled with 3D 20-node coupled-field solid elements (SOLID226). The full 3D model in ANSYS is meshed with 3,094 elements. Although the mesh of the 3D model in ANSYS is not optimized to minimize the element number, it can still be concluded that the proposed model exhibits much higher computational efficiency from the perspective of the element number.

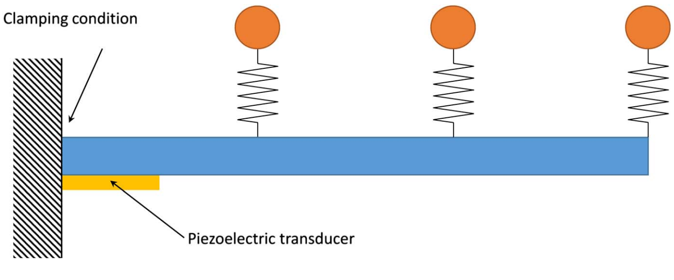

Fig. 8. Finitely long model of metamaterial beam.

The vibrations are suppressed within the local resonant gap range, as anticipated (Fig. 9). As explained previously, the shunting

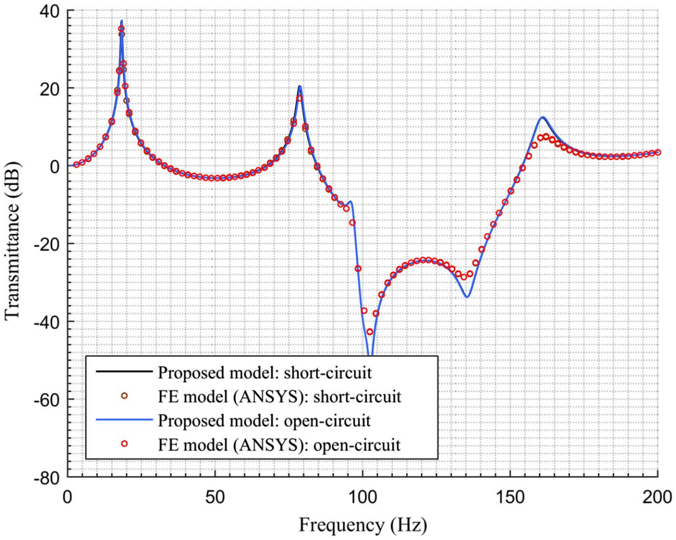

Fig. 9. Transmittances of metamaterial beam with piezoelectric transducer under short-circuit and open-circuit conditions from proposed model and FE model using ANSYS.

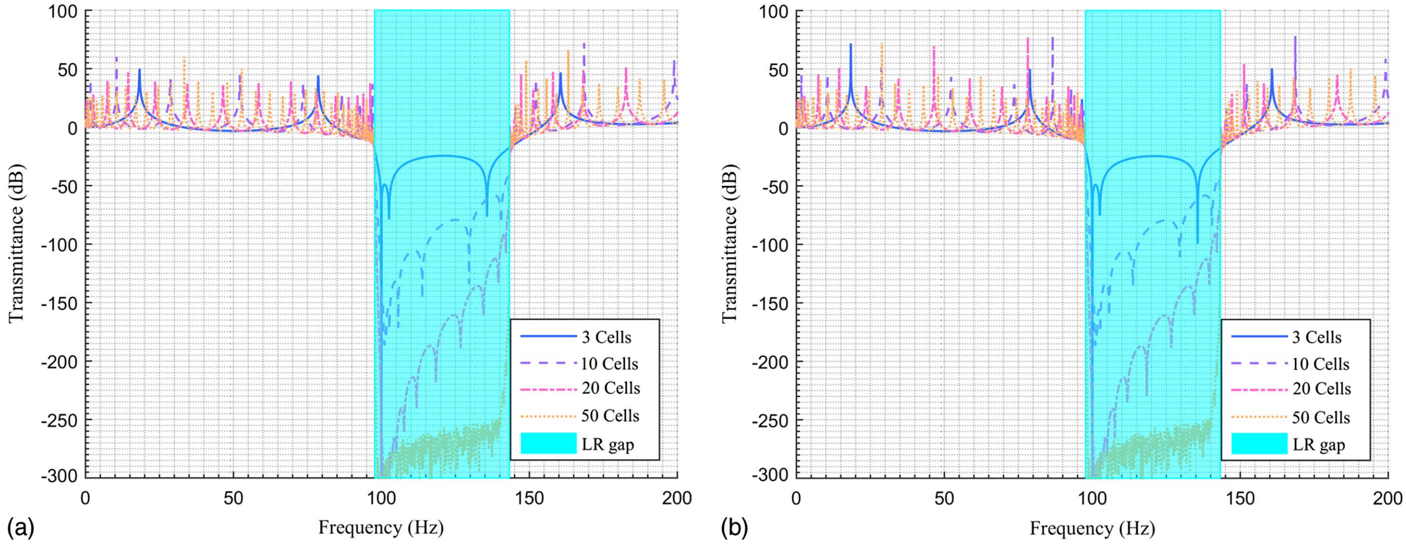

Fig. 10. Transmittances of metamaterial beams containing different number of cells: (a) under short-circuit condition; and (b) under open-circuit condition.

status of the piezoelectric transducer does not much affect the local resonant gap. The transmittance curves representing short-circuit and open-circuit conditions coincide with each other, and these curves are essentially indistinguishable. The predicted transmittances using the derived 1D elements are in good agreement with those obtained by ANSYS for the frequency range lower than the second natural frequency. However, the results show a noticeable deviation when the frequency exceeds the second natural frequency. This deviation originates from the difference between the derived 1D elements used in the proposed model and the 3D elements used in ANSYS. The global mass and stiffness matrices constructed in the proposed model and in the FE implementation in ANSYS are intrinsically different. Because the damping ratios for the first and second modes in both models are only guaranteed to be accurately equal to 0.09, only the results around first two natural frequencies are in good agreement. For higher modes, their damping ratios are out of control and possibly quite different in both models.

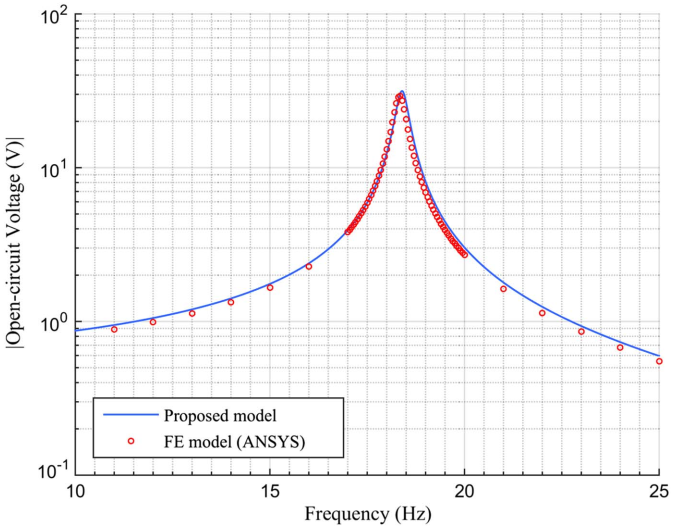

Fig. 11. Open-circuit voltage responses of metamaterial beam PEH from proposed model and FE solution from ANSYS.

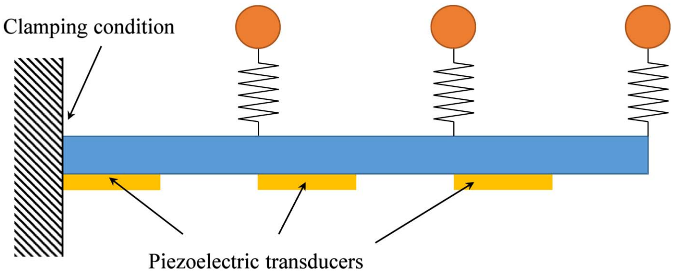

Fig. 12. Finitely long model of phononic metamaterial beam.

Both the damping and the number of resonators influence the correlation between the band structure of the infinitely long model and the transmittance of the finitely long model (Hu et al. 2017c). By removing damping and increasing the number of resonators (while keeping the same lattice constant), Figs. 10(a and b) show the transmittances of the beam containing different number of cells with the piezoelectric transducer under short-circuit and open-circuit conditions, respectively. With an increase in the number of cells, the LR gap becomes more prominent, i.e., the valley in the transmittance becomes deeper, which implies that the vibrations are more intensively suppressed. Additionally, the range of the LR gap predicted in the transmittance approaches the range predicted from the band structure. The shunting condition of the piezoelectric transducer has essentially no effect on the transmittance.

Voltage Response of Metamaterial Beam

For the same parameters used for the results in Fig. 9 and at a constant base excitation of $a_{cc} = -1\ \mathrm{m/s^2}$, Fig. 11 shows the open-circuit voltage response of the piezoelectric transducer bonded at the root of the metamaterial beam. The voltage responses from the proposed model and the FE solution (ANSYS) are provided for comparison. Although the proposed model uses only 1D elements to model the beam, the result still has sufficient accuracy (error $= 7.3\%$) compared with that obtained from the ANSYS based FE solution using 3D solid elements. The maximum open-circuit voltage amplitudes obtained from the proposed model

Downloaded from ascelibrary.org by Hong Kong University of Science and Technology (Guangzhou) on 08/02/24. Copyright ASCE. For personal use only; all rights reserved.

Downloaded from ascelibrary.org by Hong Kong University of Science and Technology (Guangzhou) on 08/02/24. Copyright ASCE. For personal use only; all rights reserved.

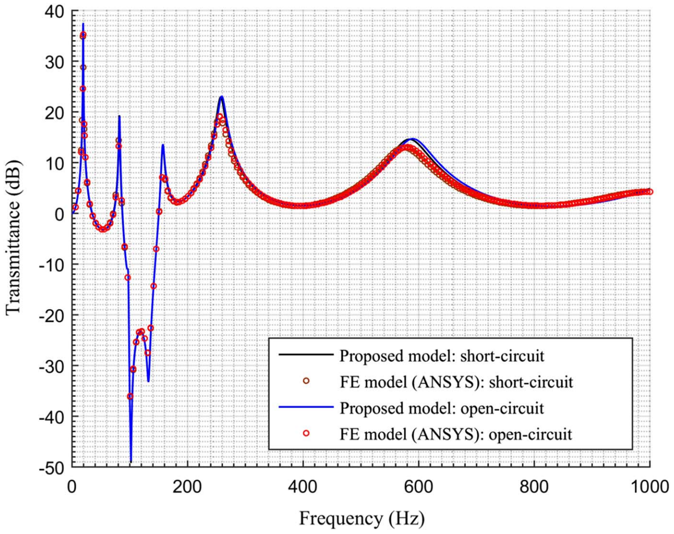

Fig. 13. Transmittances of phononic metamaterial beam with piezoelectric transducers under short-circuit and open-circuit conditions and comparison with FE solution from ANSYS.

based on 1D elements and ANSYS based on 3D solid elements are 31.5 and 29.2 V, respectively.

Transmittance of Phononic Metamaterial Beam

This section investigates the transmittances of the phononic metamaterial beam under short-circuit and open-circuit conditions. Fig. 12 shows the corresponding finitely long model of the phononic metamaterial beam in Fig. 5. The left side of the finitely long model is clamped.

For the same parameters of the host beam, resonators, piezoelectric transducers, and damping properties as those of the metamaterial beam in the previous section, Fig. 13 shows the transmittances of the phononic metamaterial beam with piezoelectric transducers under short-circuit and open-circuit conditions. In each cell of the proposed model, the subsections with and without piezoelectric coverage are both meshed with four elements. The full 3D model developed in ANSYS is meshed with 3,414 elements. Similarly, the results from the proposed model match well with those from the FE model in ANSYS. The shunting condition of the piezoelectric transducers has virtually no influence on the transmittance of the phononic metamaterial beam.

The previous section anticipated that an additional Bragg gap should appear for the phononic metamaterial beam. However, the predicted Bragg gap is not observed in Fig. 13. As was previously mentioned, both the existence of damping and number of resonators influence the transmittance of the finitely long model. By assuming the damping to be absent and increasing the number of cells, Figs. 14(a and b) show the transmittances of the beam containing different number of cells with piezoelectric transducers under short-circuit and open-circuit conditions, respectively. With an increase in the number of cells, the second valley in the transmittance becomes deeper, leading to a distinct Bragg gap. The shaded areas denote band gaps predicted from the band structure of the phononic metamaterial beam in Fig. 7(a). The band gaps predicted from the transmittances are in good agreement with those predicted from the band structures. In addition, comparing Figs. 14(a and b) shows that the shunting condition of the piezoelectric transducers does not much affect the LR gap, but affects the Bragg gap, as previously mentioned. Under the open-circuit condition, the piezoelectric effect comes into force. The mechanical impedances between the subsections with and without piezoelectric coverage have a larger difference, resulting in a widening of the Bragg gap.

Voltage Response of Phononic Metamaterial Beam

For the same parameters used for the results in Fig. 13 and at a constant base excitation of $a_{cc} = -1\ \mathrm{m/s^2}$, Fig. 15 shows the open-circuit voltage responses of the piezoelectric transducers boned onto the phononic metamaterial beam. The three piezoelectric transducers bonded from the clamped end to the free end are denoted successively the first, second, and third transducers. Fig. 15 compares the voltage responses for each of the transducers from the proposed model and the FE model (using ANSYS). The maximum open-circuit voltage amplitudes obtained from the proposed model and the FE solution (from ANSYS) are respectively 33.5 and 31.3 V for the first piezoelectric transducer, 18.2 and 16.7 V for

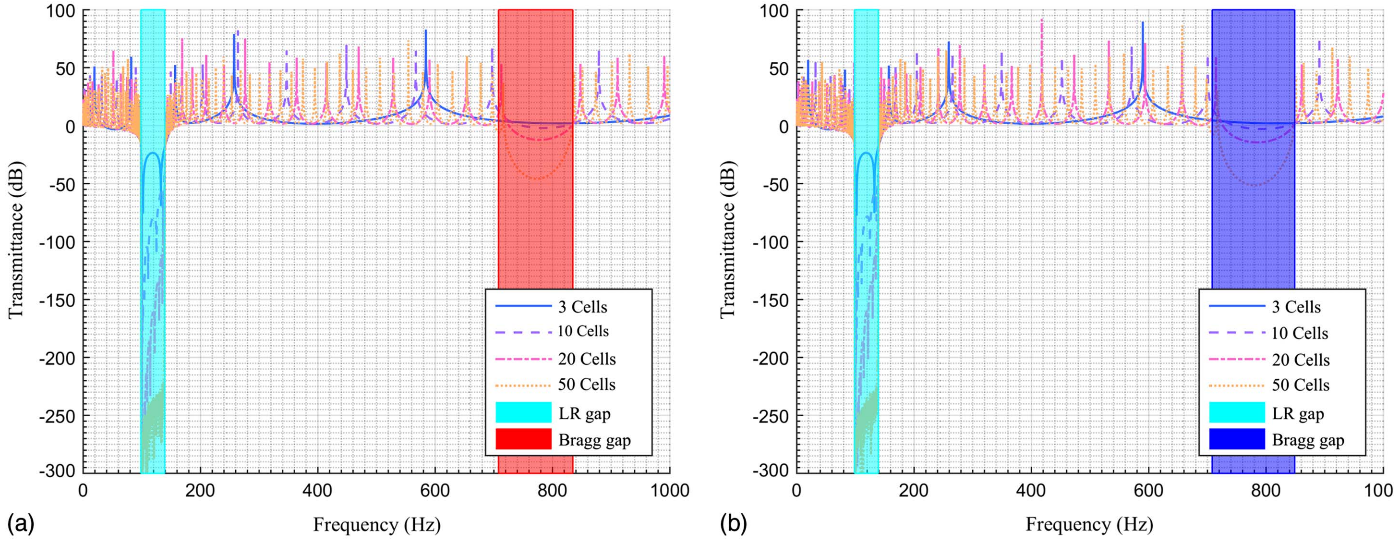

Fig. 14. Transmittances of phononic metamaterial beams containing different number of cells with piezoelectric transducers: (a) under short-circuit condition; and (b) under open-circuit condition.

J. Aerosp. Eng., 2018, 31(6): 04018088

Downloaded from ascelibrary.org by Hong Kong University of Science and Technology (Guangzhou) on 08/02/24. Copyright ASCE. For personal use only; all rights reserved.

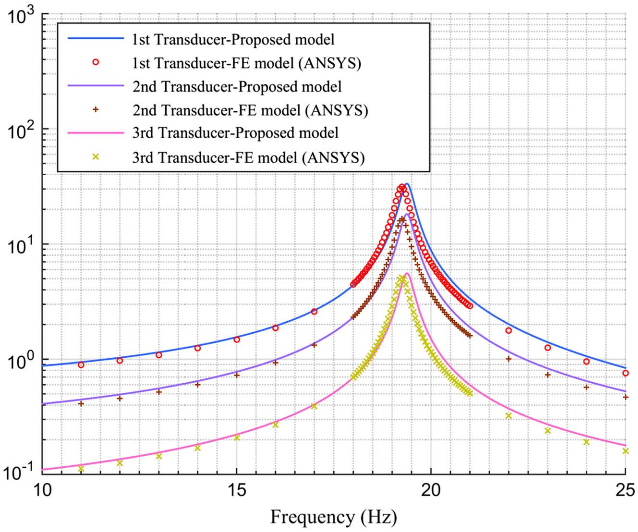

Fig. 15. Open-circuit voltage responses of phononic metamaterial beam PEH from proposed model and FE solution from ANSYS.

the second piezoelectric transducer, and 5.5 and 5.1 V for the third piezoelectric transducer. Thus, the results from the proposed model based on the derived 1D piezoelectric composite finite element have good accuracy.

Conclusions

This paper proposed a framework for modelling phononic/metamaterial beams bonded with piezoelectric transducers on the basis of a derived one-dimensional piezoelectric composite finite element for beam-type PEHs. This framework enables systematic investigation of the vibration suppression performance of phononic/metamaterial beams through evaluation of the band structures of infinitely long models or the transmittances of finitely long equivalent models. Moreover, the energy harvesting performance of phononic/metamaterial beams can be estimated by determining the open-circuit voltage responses of finitely long models. The method developed within this framework can incorporate the piezoelectric effect into consideration for calculating band structures. For piezoelectric materials with strong electromechanical coupling coefficients, the piezoelectric effect has a significant influence on the Bragg gap and thus should not be ignored.

To verify the framework and the method, two case studies were presented. The first case study investigated a conventional infinitely long model of a metamaterial beam without piezoelectric coverage. The band structure obtained from the proposed method was verified by the TMM method. For the finitely long model, a piezoelectric transducer was bonded at the clamped end of the metamaterial beam, and the transmittance and open-circuit voltage response of the piezoelectric transducer were calculated by using the proposed model. The prediction of the band gaps from the transmittances matched well with that from the band structures. Subsequently, an equivalent 3D finite element model using the ANSYS program was developed. The transmittance and open-circuit voltage response from the proposed model agreed well with the results from the FE solution from ANSYS, which further verified the proposed framework.

The second case study investigated a metamaterial beam with periodic piezoelectric coverage (i.e., a phononic metamaterial beam). For the infinitely long model, the band structures under the short-circuit and open-circuit conditions of the piezoelectric transducers were determined. This demonstrated a benefit over the existing TMM method, which cannot take the piezoelectric effect into account. For the finitely long model, the transmittance and the open-circuit voltage responses of the piezoelectric transducers were calculated using the proposed model. For both short-circuit and open-circuit conditions, the prediction of the band gaps from the transmittances agreed well with that from the band structures. Similarly, an equivalent 3D finite-element model using ANSYS was also developed for this case study to verify the results from the proposed model in relation to the transmittance and the open-circuit voltage responses of the piezoelectric transducers. The FE results correlated well with those predicted by the proposed model.

In summary, the proposed framework can be applied for investigating and designing multifunctional piezoelectric phononic/metamaterial beams.

Acknowledgments

This work is financially supported by the Energy Education Trust of New Zealand (No. 3708242) and the Ph.D. scholarship from China Scholarship Council (No. 201608250001).

References

Banerjee, A., R. Das, and E. P. Calius. 2017. “Frequency graded 1D metamaterials: A study on the attenuation bands.” *J. Appl. Phys.* 122 (7): 075101. https://doi.org/10.1063/1.4998446.

Carrara, M., M. R. Cacan, J. Toussaint, M. J. Leamy, M. Ruzzene, and A. Erturk. 2013. “Metamaterial-inspired structures and concepts for elastoacoustic wave energy harvesting.” *Smart Mater. Struct.* 22 (6): 065004. https://doi.org/10.1088/0964-1726/22/6/065004.

Chen, S., J. Wen, D. Yu, G. Wang, and X. Wen. 2011. “Band gap control of phononic beam with negative capacitance piezoelectric shunt.” *Chin. Phys. B* 20 (1): 014301. https://doi.org/10.1088/1674-1056/20/1/014301.

Chen, Z., B. Guo, Y. Yang, and C. Cheng. 2014. “Metamaterials-based enhanced energy harvesting: A review.” *Phys. B Condens. Matter* 438: 1–8. https://doi.org/10.1016/j.physb.2013.12.040.

Chen, Z., Y. Yang, Z. Lu, and Y. Luo. 2013. “Broadband characteristics of vibration energy harvesting using one-dimensional phononic piezoelectric cantilever beams.” *Phys. B Condens. Matter* 410: 5–12. https://doi.org/10.1016/j.physb.2012.10.029.

Erturk, A., and D. J. Inman. 2008. “A distributed parameter electromechanical model for cantilevered piezoelectric energy harvesters.” *J. Vib. Acoust.* 130 (4): 041002. https://doi.org/10.1115/1.2890402.

Hu, G., L. Tang, A. Banerjee, and R. Das. 2017a. “Meta-structure with piezoelectric element for simultaneous vibration suppression and energy harvesting.” *J. Vib. Acoust.* 139 (1): 011012. https://doi.org/10.1115/1.4034770.

Hu, G., L. Tang, and R. Das. 2017b. “Metamaterial-inspired piezoelectric system with dual functionalities: Energy harvesting and vibration suppression.” In *Proc., SPIE Smart Structures and Materials + Nondestructive Evaluation and Health Monitoring*. Bellingham, Washington: International Society for Optics and Photonics.

Hu, G., L. Tang, R. Das, S. Gao, and H. Liu. 2017c. “Acoustic metamaterials with coupled local resonators for broadband vibration suppression.” *AIP Adv.* 7 (2): 025211. https://doi.org/10.1063/1.4977559.

Huang, H., C. Sun, and G. Huang. 2009. “On the negative effective mass density in acoustic metamaterials.” *Int. J. Eng. Sci.* 47 (4): 610–617. https://doi.org/10.1016/j.ijengsci.2008.12.007.

Junior, C. D. M., A. Erturk, and D. J. Inman. 2009. “An electromechanical finite element model for piezoelectric energy harvester plates.” *J. Sound Vib.* 327 (1): 9–25. https://doi.org/10.1016/j.jsv.2009.05.015.

Liu, Y., D. Yu, L. Li, H. Zhao, J. Wen, and X. Wen. 2007. “Design guidelines for flexural wave attenuation of slender beams with local

Downloaded from ascelibrary.org by Hong Kong University of Science and Technology (Guangzhou) on 08/02/24. Copyright ASCE. For personal use only; all rights reserved.

resonators." *Phys. Lett. A* 362 (5): 344–347. https://doi.org/10.1016/j.physleta.2006.10.056.

Lu, M., L. Feng, and Y. Chen. 2009. "Phononic crystals and acoustic metamaterials." *Mater. Today* 12 (12): 34–42. https://doi.org/10.1016/S1369-7021(09)70315-3.

Mikoshiba, K., J. M. Manimala, and C. Sun. 2013. "Energy harvesting using an array of multifunctional resonators." *J. Intell. Mater. Syst. Struct.* 24 (2): 168–179. https://doi.org/10.1177/1045389X12460335.

Page, J., A. Sukhovich, S. Yang, M. Cowan, F. Van Der Biest, A. Tourin, and P. Sheng. 2004. "Phononic crystals." *Phys. Status Solidi B* 241 (15): 3454–3462. https://doi.org/10.1002/(ISSN)1521-3951.

Pai, P. F. 2010. "Metamaterial-based broadband elastic wave absorber." *J. Intell. Mater. Syst. Struct.* 21 (5): 517–528. https://doi.org/10.1177/1045389X09359436.

Shen, L., J. Wu, S. Zhang, Z. Liu, and J. Li. 2015. "Low-frequency vibration energy harvesting using a locally resonant phononic crystal plate with spiral beams." *Mod. Phys. Lett. B* 29 (1): 1450259. https://doi.org/10.1142/S0217984914502595.

Shu, Y., and I. Lien. 2006. "Analysis of power output for piezoelectric energy harvesting systems." *Smart Mater. Struct.* 15 (6): 1499. https://doi.org/10.1088/0964-1726/15/6/001.

Sugino, C., V. Guillot, and A. Erturk. 2017a. "Multifunctional energy harvesting locally resonant metastructures." In *Proc., ASME 2017 Conf. on Smart Materials, Adaptive Structures and Intelligent Systems*. New York: American Society of Mechanical Engineers.

Sugino, C., M. Ruzzene, and A. Erturk. 2017b. "Dynamics of hybrid mechanical-electromechanical locally resonant piezoelectric metastructures." In *Proc., ASME 2017 Conf. on Smart Materials, Adaptive Structures and Intelligent Systems*. New York: American Society of Mechanical Engineers.

Sugino, C., Y. Xia, S. Leadenham, M. Ruzzene, and A. Erturk. 2017c. "A general theory for bandgap estimation in locally resonant metastructures." *J. Sound Vib.* 406: 104–123. https://doi.org/10.1016/j.jsv.2017.06.004.

Tang, L., and Y. Yang. 2012. "A nonlinear piezoelectric energy harvester with magnetic oscillator." *Appl. Phys. Lett.* 101 (9): 094102. https://doi.org/10.1063/1.4748794.

Xu, J., and J. Tang. 2017. "Modeling and analysis of piezoelectric cantilever-pendulum system for multi-directional energy harvesting." *J. Intell. Mater. Syst. Struct.* 28 (3): 323–338. https://doi.org/10.1177/1045389X16642302.

Yang, Y., and L. Tang. 2009. "Equivalent circuit modeling of piezoelectric energy harvesters." *J. Intell. Mater. Syst. Struct.* 20 (18): 2223–2235. https://doi.org/10.1177/1045389X09351757.

Yao, S., X. Zhou, and G. Hu. 2008. "Experimental study on negative effective mass in a 1D mass-spring system." *New J. Phys.* 10 (4): 043020. https://doi.org/10.1088/1367-2630/10/4/043020.

Yu, D., Y. Liu, G. Wang, H. Zhao, and J. Qiu. 2006. "Flexural vibration band gaps in Timoshenko beams with locally resonant structures." *J. Appl. Phys.* 100 (12): 124901. https://doi.org/10.1063/1.2400803.

Zhang, S. W., J. H. Wu, and Z. P. Hu. 2013. "Low-frequency locally resonant band-gaps in phononic crystal plates with periodic spiral resonators." *J. Appl. Phys.* 113 (16): 163511. https://doi.org/10.1063/1.4803075.

Zhu, R., X. Liu, G. Hu, C. Sun, and G. Huang. 2014. "A chiral elastic metamaterial beam for broadband vibration suppression." *J. Sound Vib.* 333 (10): 2759–2773. https://doi.org/10.1016/j.jsv.2014.01.009.

J. Aerosp. Eng., 2018, 31(6): 04018088